Title

Experimental observations and numerical modeling of lipid-shell microbubbles with calcium-adhering moieties for minimally-invasive treatment of urinary stones

Permalink

Journal

ISSN

Authors

Pishchalnikov, Yuri A
Behnke-Parks, William
Maeda, Kazuki
et al.

Publication Date

DOI

Peer reviewed

Experimental observations and numerical modeling of lipid-shell microbubbles with calcium-adhering moieties for minimally-invasive treatment of urinary stones

Yuri A. Pishchalnikov, William Behnke-Parks, Kazuki Maeda, et al.

ARTICLES YOU MAY BE INTERESTED IN

Experimental observations and numerical modeling of lipid-shell microbubbles with calcium-adhering moieties for minimally-invasive treatment of urinary stones

Yuri A. Pishchalnikov
R&D, Applaud Medical, Inc., San Francisco, CA, 94107; yurapish@gmail.com

William Behnke-Parks
Applaud Medical, Inc., San Francisco, CA, 94107; will.parks@applaudmedical.com

Kazuki Maeda
Department of Mechanical Engineering, University of Washington, Seattle, WA, 98105; maeda@uw.edu

Tim Colonius
Division of Engineering and Applied Science, California Institute of Technology, Pasadena, CA, 91125; colonius@caltech.edu

Matthew Mellema, Matthew Hopcroft and Alice Luong
Applaud Medical, Inc., San Francisco,CA, 94107; matt.mellema@applaudmedical.com, matt.hopcroft@applaudmedical.com, alice.luong@applaudmedical.com

Scott Wiener and Marshall L. Stoller
Department of Urology, University of California, San Francisco, CA, 94143; svwiener@gmail.com, Marshall.Stoller@ucsf.edu

Thomas Kenny
Department of Mechanical Engineering, Stanford University, Stanford, CA, 94305; kenny@cdr.stanford.edu

Daniel J. Laser
Applaud Medical, Inc., San Francisco, CA 94107; daniel.laser@applaudmedical.com

A novel treatment modality incorporating calcium-adhering microbubbles has recently entered human clinical trials as a new minimally-invasive approach to treat urinary stones. In this treatment method, lipid-shell gas-core microbubbles can be introduced into the urinary tract through a catheter. Lipid moities with calcium-adherance properties incorporated into the lipid shell facilitate binding to stones. The microbubbles can be excited by an extracorporeal source of quasi-collimated ultrasound. Alternatively, the microbubbles can be excited by an intraluminal source, such as a fiber-optic laser. With either excitation technique, calcium-adhering microbubbles can significantly increase rates of erosion, pitting, and fragmentation of stones. We report here on new experiments using high-speed photography to characterize microbubble expansion and collapse. The bubble geometry observed in the experiments was used as one of the initial shapes for the numerical modeling. The modeling showed that the bubble dynamics strongly depends on bubble shape and stand-off distance. For the experimentally observed shape of microbubbles, the numerical modeling showed that the collapse of the microbubbles was associated with pressure increases of some two-to-three orders of magnitude compared to the excitation source pressures. This in-vitro study provides key insights into the use of microbubbles with calcium-adhering moieties in treatment of urinary stones.

1.   INTRODUCTION

Stone-adhering microbubbles[1] have recently entered human clinical trials as a medical device for minimally invasive approach to treat urinary stones. Gas-filled microbubbles are introduced through a catheter and adhere to urinary stones with calcium-adhering moieties incorporated into encapsulating lipid shells.[1–3] The microbubbles can be excited either minimally invasively (e.g., with a laser coupled to an optical fiber delivered through the ureter via a ureteroscope) or non-invasively with an extracorporeal source of ultrasound(Fig. 1).[1] With either excitation technique, recent studies suggest that the stone-adhering microbubbles can significantly increase the breakage of urinary stones.[2,3] To better understanding the mechanisms of action of microbubbles in treatment of urinary stones, here we studied the dynamics of microbubbles at the surface of urinary stones *in vitro*. This study is a continuation of the work presented at the previous 175th meeting of the Acoustical Society of America.[4] The microbubbles were driven with quasi-collimated ultrasound at low intensities and studied using a high-speed video microscopy. The observed bubble geometry and the stand-off distance were used as input parameters for the numerical modeling of the collapsing bubbles. The modeling showed that the collapse of stone-adhering microbubbles can produce pressure spikes with amplitudes significantly greater than the amplitude of the driving acoustic waves.
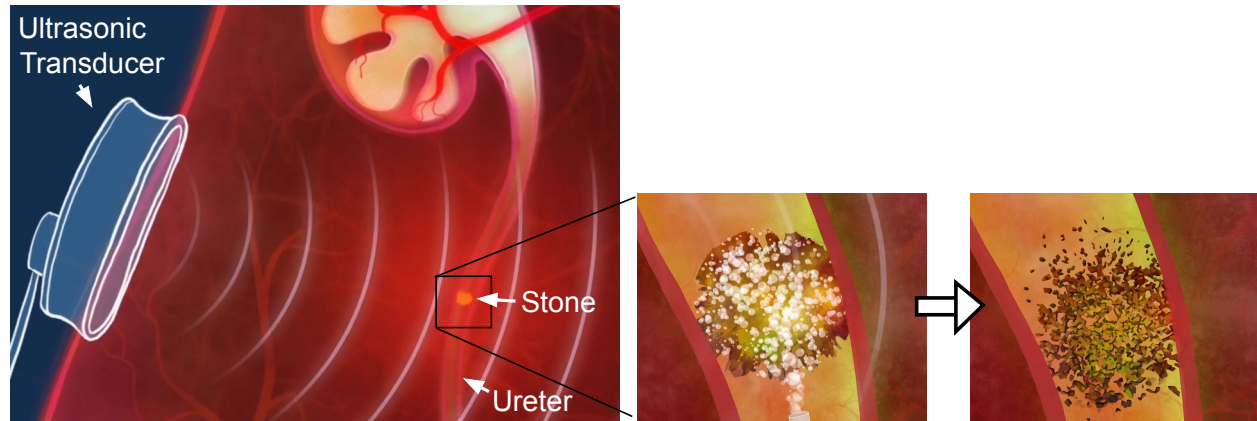
Figure 1:   The concept of treating urinary stones using microbubbles with calcium-adhering moieties. Gas-filled microbubbles are introduced into the urinary tract through a catheter and adhere to an urinary stone (middle). The adhered microbubbles are excited with an extracorporeal source of quasi-collimated ultrasound and erode the stone facilitating its passage through the urinary tract.

2.   MATERIALS AND METHODS

A.   LIPID-SHELL MICROBUBBLES AND URINARY STONES

Stone-adhering microbubbles (Applaud Medical, Inc.) were made of perfluoroalkane gas $\left(C_4F_{10}\right)$ encapsulated into lipid shells with calcium-adhering moieties.[1–3] The chemical composition of the moieties was based on a synthetic pyrophosphate analog structure conferring adhering affinity for calcium constituents of urinary stones.

These experiments were conducted with surgically retrieved calcium-oxalate-monohydrate urinary stones. The stones were hydrated in deionized water and positioned in the test tank to study the dynamics of microbubbles with a high-speed video microscopy (Fig. 2).

B.   HIGH-SPEED VIDEO MICROSCOPY

Bubble dynamics was captured using a high-speed (HS) camera Shimadzu Hyper Vision HPV-X2 (Shimadzu, Kyoto, Japan). The camera had a burst image sensor FTCMOS2 with ISO sensitivity of 16,000 and a monochrome 10-bit resolution. The camera recorded 400- by 250-pixel frames either in FP or HP mode. The FP mode captured every pixel recording 128 frames at a rate up to five million frames per second (Mfps). The HP mode captured every other pixel interpolating the images to 400- by 250-pixel frames and recording 256 frames at a rate up to 10 Mfps. The physical size of sensor pixels was 32 by 32 μm.

The high-speed camera was used with a Nikon Eclipse TS100 microscope with a $4\times$ objective ($4\times$/0.13 PhL DL, WD 16.4, Nikon Plan Fluor), a $2.5\times$ projection lens (Nikon CF PL2.5$\times$), and a 34-cm extension tube (Thorlabs Inc., Newton, NJ, USA). The optical magnification was determined using a metallized hemacytometer (Hausser Bright-Line, Hausser Scientific, Horsham, PA, USA) and was 1 μm per pixel.

Nikon Eclipse TS100 microscope had inverted configuration in which the objective was positioned at the bottom. To use this configuration, a test tank had a transparent glass window at the bottom of the tank (Fig. 2). The window was made of a microscope slide ($75\times25\times1$ mm, VistaVision, VWR International, LLC, Radnor, PA) glued along its edges to the bottom of the tank. The tank was 3-D printed from a thermoplastic material—acrylonitrile butadiene styrene—and covered with a waterproof coating (Marine Grade Epoxy 109 Medium, Tap Plastics, CA, USA). The test tank was filled with six liters of water (PURELAB Chorus 1 for Life Science Applications, ELGA, Veolia Water Solutions and Technologies, UK) with an electrical resistivity of 18.2 MOhm-cm and the ultrafiltration to particle size less than 0.05 μm. The water remained in the tank for several days and was in equilibrium with atmospheric gases.

We used both continuous and flashlight illumination. The continuous lighting was provided by a fluorescence illumination system EXFO X-cite 120 (XE120, Photonic Solutions Inc., Mississauga, Ontario, CA). This light source used a 120-W Metal Halide lamp coupled to a liquid lightguide. The end of the lightguide was positioned at about 1 cm above the stone to backlit the stone (Fig. 2). The side lighting was provided by a flashlamp WRF300 (Hadland Imaging LLC, Santa Cruz, CA). This spark-discharge lamp produced a light pulse with the duration of about 10 μs. The spark light was delivered through a liquid lightguide illuminating the side of the stone proximal to the incoming acoustic waves (Fig. 2).

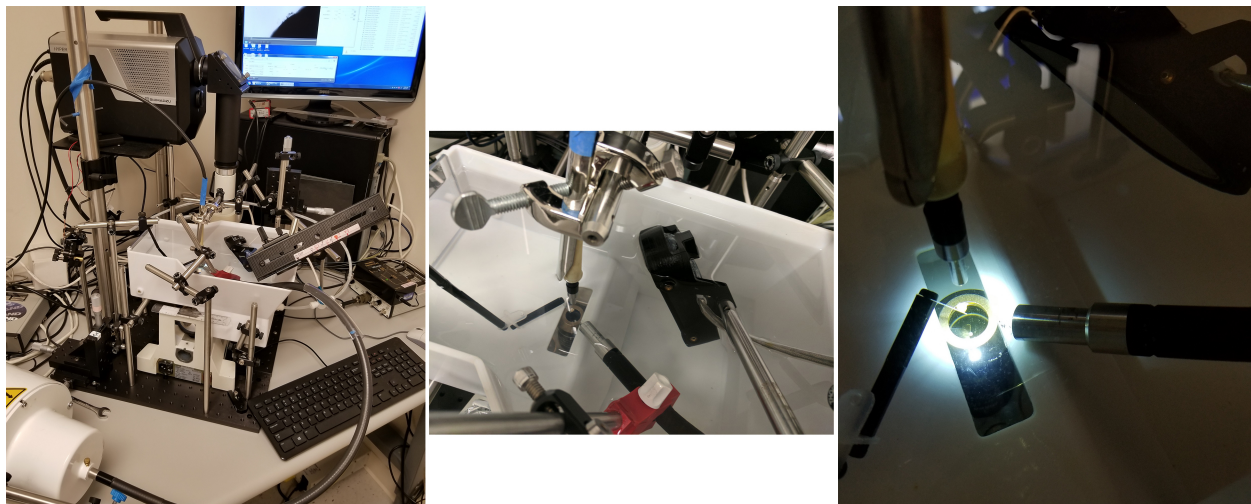***Figure 2: Experimental setup. Left: general view with the HS-camera (top left), the spark-light source (bottom left), and the water test tank positioned over the inverted microscope (center). Middle: view in the test tank. Right: zoomed up view of an urinary stone positioned at the focus of the microscope. Back- and side-illumination was provided by two liquid lightguides positioned at about 1 cm from the stone.***

C.   DRIVING ACOUSTIC WAVES

Driving acoustic waves were generated with a custom-made piezo-electric transducer (manufactured for Applaud Medical by Sonic Concepts, Inc., Bothell, WA). The active element of the transducer was made of a piezo-electric plate (72.3×30.3×3.18 mm) divided into eight elements and connected in pairs. Each pair was driven by one of the four controllable power amplifiers (AP-400B, ENI, USA). The frequency and duration of the acoustic bursts were computer controlled by a specially designed signal generator, allowing us to not only reproduce the frequency modulation used in the clinic but also to study other driving regimes. In this work, the acoustic bursts were generated with a frequency set of 400, 400, 433, and 433 kHz.

Acoustic waves were measured using a needle hydrophone with a frequency range of 50 kHz–1.9 MHz (Y-104, Sonic Concepts, Inc., Bothell, WA). The sensitive element of the hydrophone was a ceramic crystal with a diameter of 1.5 mm. The sensitive element was embedded at the rounded tip of the hydrophone enclosed in a metal tube with a diameter of 3 mm. As the diameter of the tip was comparable with the wavelength of acoustic waves ($\sim 3.4 - 3.8$ mm), the hydrophone sensitivity depended on hydrophone's orientations and was about 6 V/MPa for the normal angle of incidence of acoustic waves. The angular response of the hydrophone was measured and taken into account in these measurements. The uncertainty of pressure measurements was estimated to be on the order of 30%. Another uncertainty was related to the scattering of acoustic waves by the irregular surface of the urinary stone. As the characterization of wave scattering was beyond the scope of this report, the driving acoustic pressure was measured without the stone by positioning the sensitive tip of the hydrophone at the focus of the microscope. The pressure at the stone, however, could be greater due to reflection of pressure waves from the nearly rigid surface of the stone.

A typical trace of the hydrophone is shown in Fig. 3. The central frequency of the driving acoustic bursts was 416.5 kHz with the duration of the beat envelope of ~ 30 μs. During the first four acoustic cycles ($\sim 90 - 100$ μs), the driving pressure increased reaching a pressure amplitude of $\sim 1.5 \pm 0.5$ MPa. The increase of the driving acoustic pressure was associated with the growth of bubbles to a larger size from cycle to cycle. The collapse of the larger bubbles could produce daughter microbubbles that became visible in the subsequent acoustic cycles. In this study, we focus on the dynamics of a single microbubble during one acoustic cycle marked by a red rectangle starting at ~ 95 μs and lasting for a period of 2.4 μs (Fig. 3).
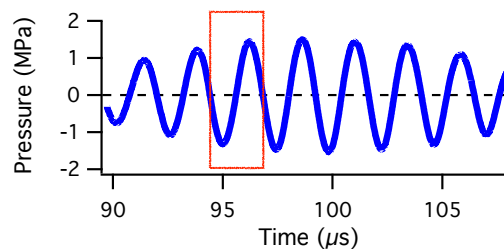

Figure 3:   *The driving acoustic pressure measured with a hydrophone positioned at the focus of the microscope. The red rectangle marks the acoustic period shown in HS-camera movies (Figs. 4 and 5).*

D.   NUMERICAL MODELING

The collapse of the gas bubble in the liquid was simulated using a compressible multi-component flow solver.[5] In the solver, an anti-diffusion based interface sharpening technique[6] was used to suppress numerical diffusion of the gas-liquid interface. We neglect viscosity, surface tension, and heat and mass transfer across the gas-liquid interface. The bubble was assumed to remain axisymmetric. The stone was modeled as an acoustically-rigid infinite plane wall. Both fluids were initially at rest, assuming that the bubble was fully expanded before its collapse. The initial pressure of the liquid was set to $P_\infty = 1.55$ MPa. The initial pressure and density of the gas, the shape of the bubble, and its stand-off distance from the wall were varied.

3.   RESULTS

A.   HIGH-SPEED VIDEO MICROSCOPY OF BUBBLE DYNAMICS

Figures 4 and 5 show typical growth-collapse cycles of representative microbubbles at the surface of an urinary stone. These sequences of images were recorded with the high-speed camera during one acoustic cycle of the driving wave marked by the red rectangle in Fig. 3. Under these driving conditions, microbubbles grew to several tens of micrometers. The bubble in Fig. 5 was smaller and collapsed earlier than the bubble in Fig. 4. Among hundreds of microbubbles observed in this system over the course of months of experiments, the vast majority exhibit a slightly non-spherical shape at their maximum expansion similar to that seen in the $t \sim 1\,\mu$s frames in Figs. 4 and 5, with a cross-section well modeled as an ellipse.

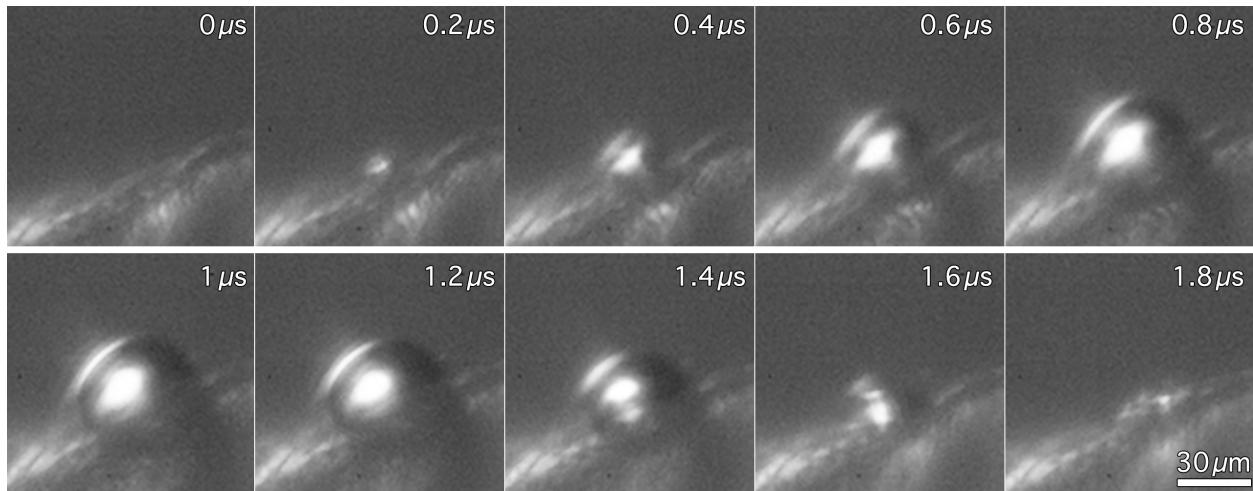*Figure 4: High-speed imaging of the growth (top row) and collapse (bottom row) of a bubble at the surface of an urinary stone during one acoustic cycle recorded in FP mode at 5 Mfps and 100-ns exposure.*
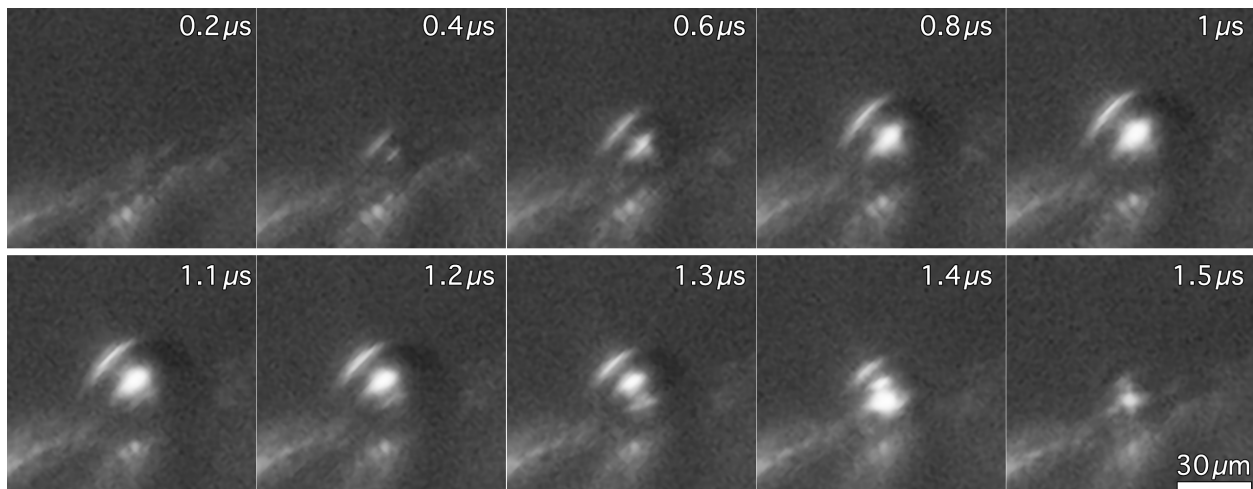

Figure 5: High-speed imaging of the growth and collapse of a bubble recorded in HP mode at 10 Mfps and 50-ns exposure. The bubble growth (top row) is shown at 0.2-μs step skipping every other frame.

B.   NUMERICAL MODELING

We modeled the collapse approximating the initial shape of the bubble as an oblate spheroid (major semi-axis of 31 μm, minor semi-axis of 20 μm, and the stand-off distance of 12 μm) with two initial gas pressures ($P_{01} = 10$ Pa and $P_{02} = 7$ kPa) representing low and high gas content in the bubble (Fig. 6). The pressure P_{01} was chosen by approximating that the bubble filled with ambient air was polytropically expanded from about 1.2 to 26 μm radius; the pressure P_{02} would occur in the expanded bubble filled with water vapor at $\sim 39°$C.
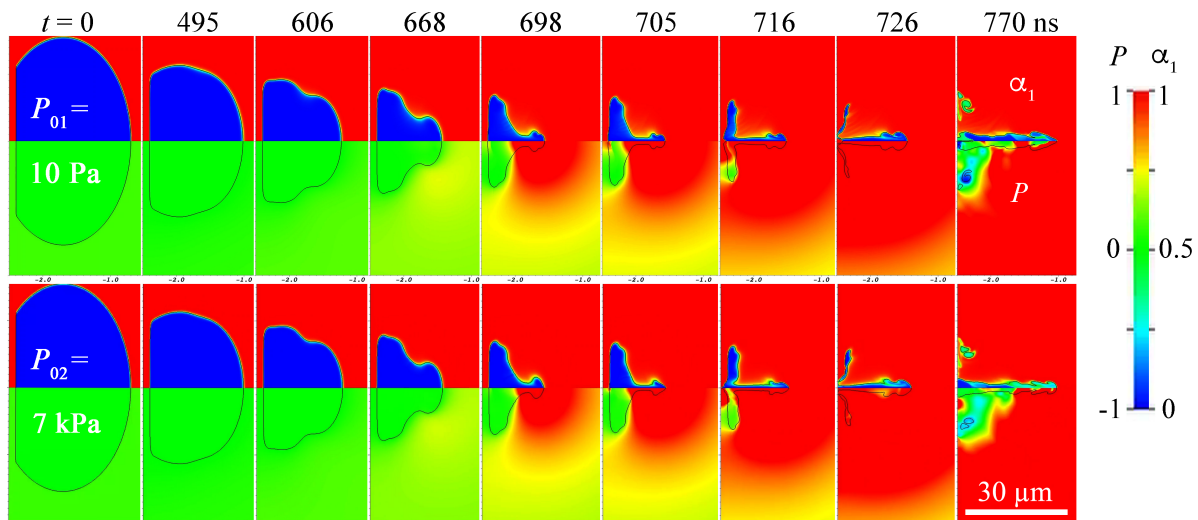

Figure 6: *Two simulations of bubbles collapsing with different initial gas pressure of $P_{01} = 10$ Pa (top) and $P_{02} = 7$ kPa (bottom) representing low and high gas content in the bubble. The top halves show the volume fraction of liquid α_1; the bottom halves show the pressure P. The black contour lines are drawn at the volume fraction of $\alpha_1 = 50\%$ suggesting the position of the liquid-gas interface. The stone was modeled as a rigid surface located along the left boundary of the simulation domain, initially separated from the microbubbles by a thin layer of liquid.*
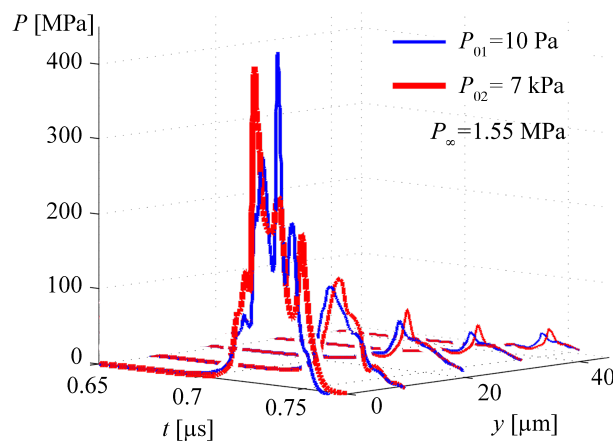
Figure 7: *Pressure P vs time t at five lateral distances y along the stone surface for the two simulations shown in Fig. 6. The radial distance $y = 0$ corresponds to the axis of symmetry of the bubble. Regardless of the initial gas pressure in the bubble (P_{01} and P_{02}), the bubbles produced pressure pulses with an amplitude about two-to-three orders of magnitude greater than the driving pressure of $P_{\infty} = 1.55$ MPa.*

Despite the three-orders-of-magnitude difference in the gas content of the bubbles (10 Pa vs 7 kPa), the bubbles show similar dynamics (Fig. 6) and produced similar pressures at the stone surface (Fig. 7). The bubble dynamics, however, strongly depended on the initial shape and stand-off distance (Fig. 8).
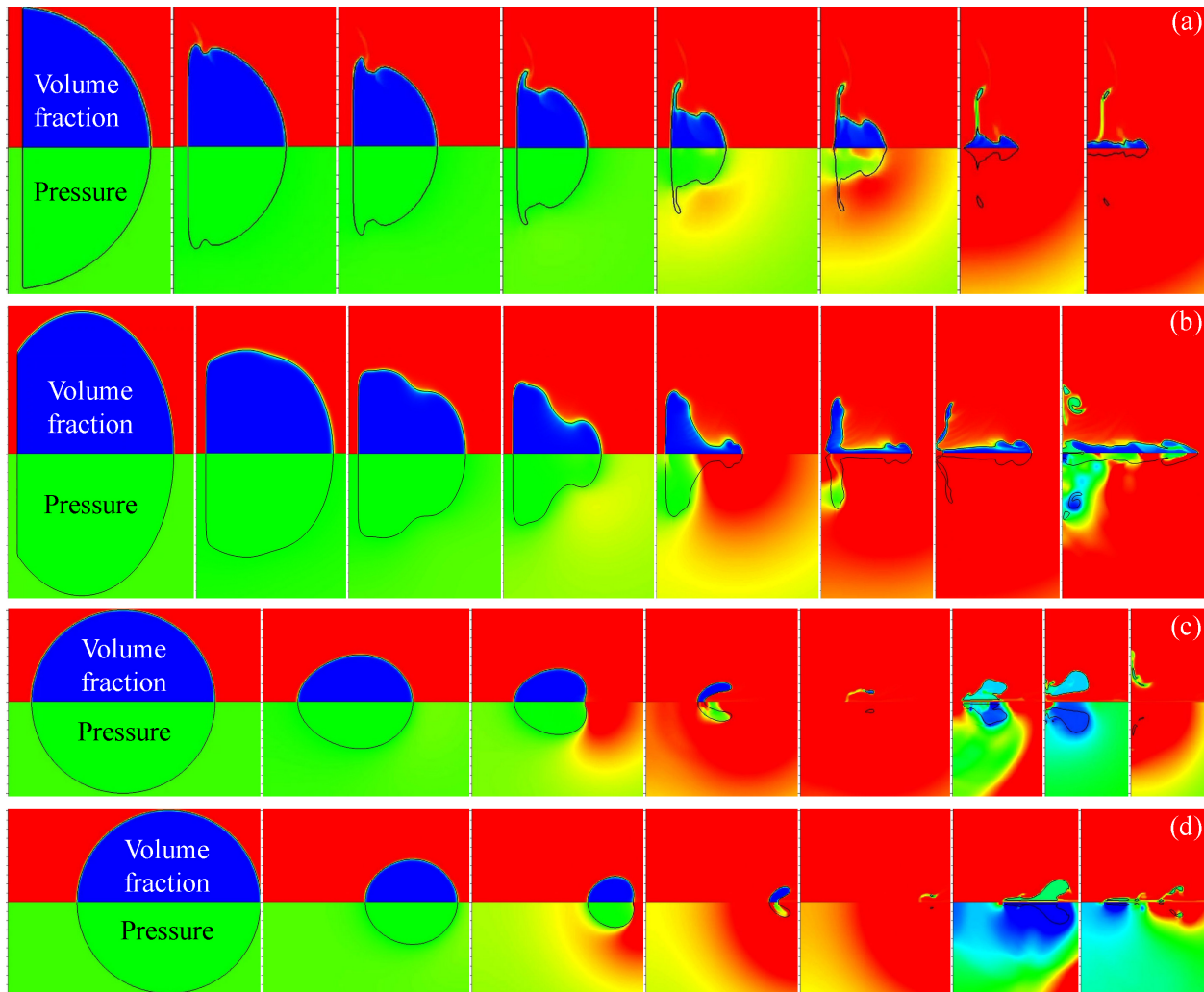

Figure 8: Numerical simulations of the collapse of the bubble with the initial shape of a hemisphere (a), an oblate spheroid (b), and a sphere at stand-off distances of 1.25 (c) and 1.75 (d). The hemispherical bubble and the oblate spheroid collapsed with a circumferential constriction pinching the bubbles. The initially spherical bubbles transformed into an egg shape but did not exhibit the circumferential pinching. For the initially spherical bubbles, the dominant feature of the collapse was the formation of an axial jet directed toward the rigid surface (located on the left). The initial gas pressure in the bubbles was 10 Pa.

Figure 8 shows the collapse of the bubbles with three distinct initial geometries: a hemisphere (a), an oblate spheroid (b), and a sphere with the stand-off distances of 1.25 (c) and 1.75 (d). The hemispherical bubble and the bubble with the initial shape of an oblate spheroid were collapsing mainly in the direction toward the axis of symmetry of the bubble with a circumferential narrowing pinching the bubbles. The spherical bubble collapsed without the pinching even though the flow of liquid toward the axis of symmetry deformed the sphere into the egg shape at the beginning of the collapse. Later during the collapse the axial jet dominated the dynamics of the collapse of the initially spherical bubbles.

4.   DISCUSSION

Kornfeld and Suvorov were among the first showing that cavitation bubbles growing and collapsing at a rigid surface are non-spherical.[7] More recently, lipid-shell microbubbles adherent to a flexible cellulose boundary were observed to oscillate asymmetrically acquiring an ellipsoidal shape,[8] similar to the bubble shape observed in the present study with microbubbles at the surface of urinary stones.

The present high-speed video observations showed that stone-adhering microbubbles driven by ultrasound at sub–MHz frequencies with pressure amplitude on the order of 1.5 MPa (Fig. 3) can grow to tens of micrometer in size (Figs. 4 and 5) and violently collapse. Although the direct measurements of pressure produced by the collapsing bubbles is difficult,[9–11] the numerical modeling of the collapse suggests that the bubbles can produce pressures on the order of 0.5 GPa (Fig. 7). Hence, these results suggest that the collapsing microbubbles can produce local pressures two-to-three orders of magnitude greater than the amplitude of the driving wave.

For comparison, this pressure amplitude is greater than peak positive pressures generated in the focus of shock wave lithotripters. In shock wave lithotripsy, to break urinary stones the shock pulses have peak positive pressure of 15–120 MPa.[12–24] This positive-pressure phase of the lithotripter pulse is followed by the negative-pressure phase with a tensile stress of 5–20 MPa. The tensile stress causes an inertial growth of cavitation bubbles that collapse usually hundreds of microseconds after the passage of the lithotripter pulse.[22–29] Therefore, cavitation bubbles in shock wave lithotripsy collapse under a static pressure of 0.1 MPa. In comparison, the collapse of the stone-adhering microbubbles considered here was intensified by the positive-pressure phase of the driving acoustic wave with the amplitude of ∼1.5 MPa.

Further, the lithotripter shock pulses have a total duration of ∼ 10 μs and are typically administered at pulse repetition frequencies (PRFs) of 0.5–2 Hz.[13–30] Moreover, it has been shown that stone breakage at 2 Hz PRF was significantly reduced in comparison with stone breakage at 0.5 Hz.[31–34] In comparison with shock wave lithotripsy, the stone-adhering microbubbles driven with acoustic bursts can produce thousands of collapses per second.

One caveat to the present numerical results is that mass transfer was not modeled. To assess the extent to which the gas content may influence bubble dynamics, we modeled the collapse with two initial gas pressures: $P_{01} = 10$ Pa and $P_{02} = 7000$ Pa. The pressure P_{02}, which is the vapor pressure at ∼ 39°C, was likely a representation of high gas content in the bubble. The modeling showed, however, that both bubbles had similar dynamics during the collapse (Fig. 6) and produced similar pressures at the rigid surface (Fig. 7). Specifically, the peak pressure produced by the collapsing bubbles at the rigid wall was 445 MPa at P_{01} and 421 MPa at P_{02} (Fig. 7). Hence, this numerical modeling suggests that the gas content in this range did not substantially affect the results.

In the present modeling, we did not assess the influence of the grid resolution. We plan on refining the grid resolution by using an adaptive mesh refinement approach.[35,36]

Here the stone was modeled as an acoustically rigid plane wall neglecting elasticity and geometry of urinary stones. It has been shown, however, that both factors influence the dynamics of bubbles.[37,38] Furthermore, in this work the driving acoustic field was measured without the stone in place. It is reasonable to anticipate that the actual pressure field at the stone would be influenced by the scattering of the acoustic waves from the stone. The geometry of the hydrophone, however, did not allow us using the hydrophone for acoustic measurements at the stone without affecting the acoustic field. Here, the driving pressure was modeled as a pressure step with a constant pressure P_∞ at large distances from the bubble.

The driving transducer was submerged in the water tank providing almost ideal transmission of the acoustic waves. It has been observed with dry-head lithotripters that the coupling gel could trap air pockets diminishing the transmission of acoustic energy to the target.[23,39–43] The investigation of the extent to which the above effects may affect the acoustic field was beyond the scope of this report.

5. CONCLUSION

In summary, we used high-speed video microscopy to observe the dynamics of microbubbles at the surface of urinary stones *in vitro*. Microbubbles, driven by acoustic bursts with sub-MHz central frequencies and ∼1.5 MPa pressure amplitudes, expanded to tens of micrometers in diameter and were non-spherical. The bubble geometry observed in the high-speed camera observations was used as the initial shape for the numerical modeling. The modeling showed that microbubbles collapsing at the rigid surface produced pressure spikes two-to-three orders of magnitude greater than the amplitude of the driving wave. This focusing ability of stone-adhering microbubbles can enable stone-treatment modalities with driving pressures significantly lower than those required without stone-adhering microbubbles.

ACKNOWLEDGMENTS

REFERENCES

[1] K. Ramaswamy, V. Marx, D. Laser, T. Kenny, T. Chi, M. Bailey, M. D. Sorensen, R. H. Grubbs, and M. L. Stoller, BJU Int. **116**, 9 (2015).

[2] M. Mellema, W. Behnke-Parks, A. Luong, M. Hopcroft, C. Mills, S. Ho, R. Hsi, D. Laser, T. Kenny, R. Grubbs, and M. Stoller, J. Urol. **199**, e479 (2018).

[3] S. Wiener, M. Mellema, Y. Pishchalnikov, W. Behnke-Parks, D. Laser, and M. Stoller, J. Urol. **199**, e322 (2018).

[4] Y. A. Pishchalnikov, W. Behnke-Parks, M. Mellema, M. Hopcroft, A. Luong, T. Colonius, K. Maeda, K. Morrison, and D. Laser, J. Acoust. Soc. Am. **143**, 1861 (2018).

[5] V. Coralic and T. Colonius, J. Comput. Phys. **274**, 95 (2014).

[6] K.-M. Shyue and F. Xiao, J. Comput. Phys. **268**, 326 (2014).

[7] M. Kornfeld and L. Suvorov, J. Appl. Phys. **15**, 495 (1944).

[8] S. Zhao, K. W. Ferrara, and P. A. Dayton, Appl. Phys. Lett. **87**, 134103 (2005).

[9] Z. Q. Wang, R. Pecha, B. Gompf, and W. Eisenmenger, Phys. Rev. E **59**, 1777 (1999).

[10] R. Pecha and B. Gompf, Phys. Rev. Lett. **84**, 1328 (2000).

[11] Y. A. Pishchalnikov, J. Gutierrez, W. W. Dunbar, and R. W. Philpott, Ultrasonics **65**, 380 (2016).

[12] M. R. Bailey, T. J. Matula, O. A. Sapozhnikov, R. O. Cleveland, Y. A. Pishchalnikov, and J. A. McAteer, AIP Conf. Proc. **829**, 380 (2006).

[13] R. O. Cleveland, M. R. Bailey, N. Fineberg, B. Hartenbaum, M. Lokhandwalla, J. A. McAteer, and B. Sturtevant, Rev. Sci. Instrum. **71**, 2514 (2000).

[14] O. A. Sapozhnikov, V. A. Khokhlova, M. R. Bailey, J. C. Williams, J. A. McAteer, R. O. Cleveland, and L. A. Crum, J. Acoust. Soc. Am. **112**, 1183 (2002).

[15] Y. A. Pishchalnikov, O. A. Sapozhnikov, M. R. Bailey, I. V. Pishchalnikova, J. C. Williams, and J. A. McAteer, Acoust. Res. Lett. Online **6**, 280 (2005).

[16] Y. A. Pishchalnikov, J. A. McAteer, R. J. VonDerHaar, I. V. Pishchalnikova, J. C. Williams, and A. P. Evan, J. Urol. **176**, 2294 (2006).

[17] R. K. Handa, J. A. McAteer, L. R. Willis, Y. A. Pishchalnikov, B. A. Connors, J. Ying, J. E. Lingeman, and A. P. Evan, BJU Int. **99**, 1134 (2007).

[18] A. P. Evan, J. A. McAteer, B. A. Connors, Y. A. Pishchalnikov, R. K. Handa, P. Blomgren, L. R. Willis, J. C. Williams, J. E. Lingeman, and S. Gao, BJU Int. **101**, 382 (2008).

[19] B. A. Connors, J. A. McAteer, A. P. Evan, P. M. Blomgren, R. K. Handa, C. D. Johnson, S. Gao, Y. A. Pishchalnikov, and J. E. Lingeman, BJU Int. **110**, 1376 (2012).

[20] Y. A. Pishchalnikov, J. A. McAteer, R. J. VonDerHaar, I. V. Pishchalnikova, and J. C. Williams, in *AIP Conf. Proc.*, Vol. 1049 (AIP, 2008) pp. 238–242.

[21] Y. A. Pishchalnikov, J. A. McAteer, J. C. Williams, B. A. Connors, R. K. Handa, J. E. Lingeman, and A. P. Evan, J. Endourol. **27**, 631 (2013).

[22] T. J. Matula, P. R. Hilmo, B. D. Storey, and A. J. Szeri, Phys. Fluids **14**, 913 (2002).

[23] M. R. Bailey, J. A. Mcateer, Y. A. Pishchalnikov, M. F. Hamilton, and T. Colonius, Acoust. Today **2**, 18 (2006).

[24] Y. A. Pishchalnikov, J. A. McAteer, and J. C. Williams, BJU Int. **102**, 1681 (2008).

[25] C. C. Church, J. Acoust. Soc. Am. **86**, 215 (1989).

[26] Y. A. Pishchalnikov, O. A. Sapozhnikov, M. R. Bailey, J. C. Williams, R. O. Cleveland, T. Colonius, L. A. Crum, A. P. Evan, and J. A. McAteer, J. Endourol. **17**, 435 (2003).

[27] M. R. Bailey, Y. A. Pishchalnikov, O. A. Sapozhnikov, R. O. Cleveland, J. A. McAteer, N. A. Miller, I. V. Pishchalnikova, B. A. Connors, L. A. Crum, and A. P. Evan, Ultrasound Med. Biol. **31**, 1245 (2005).

[28] W. Kreider, L. A. Crum, M. R. Bailey, and O. A. Sapozhnikov, J. Acoust. Soc. Am. **130**, 3531 (2011).

[29] Y. A. Pishchalnikov, J. C. Williams, and J. A. McAteer, J. Acoust. Soc. Am. **130**, EL87 (2011).

[30] Y. A. Pishchalnikov, M. M. Kaehr, and J. A. Mcateer, in *Vol. 2 Biomed. Biotechnol. Eng.* (ASME, 2007) pp. 191–200.

[31] R. F. Paterson, D. A. Lifshitz, J. E. Lingeman, A. P. Evan, B. A. Connors, N. S. Fineberg, J. C. Williams, and J. A. McAteer, J. Urol. **168**, 2211 (2002).

[32] K. T. Pace, D. Ghiculete, M. Harju, and R. J. Honey, J. Urol. **174**, 595 (2005).

[33] Y. A. Pishchalnikov, J. A. McAteer, J. C. Williams, I. V. Pishchalnikova, and R. J. VonDerHaar, J. Endourol. **20**, 537 (2006).

[34] J. A. McAteer, A. P. Evan, B. A. Connors, Y. A. Pishchalnikov, J. C. Williams, and J. E. Lingeman, in *AIP Conf. Proc.*, Vol. 1049 (AIP, 2008) pp. 243–248.

[35] K. Schmidmayer, A. Marty, F. Petitpas, and E. Daniel, in *53rd 3AF Int. Conf. Appl. Aerodyn.* (Salon-de-Provence, France, 2018) pp. hal–01781830.

[36] K. Schmidmayer, F. Petitpas, and E. Daniel, J. Comput. Phys. , Under revisions (2018).

[37] Y. Tomita, P. B. Robinson, R. P. Tong, and J. R. Blake, J. Fluid Mech. **466**, 259 (2002).

[38] C. K. Turangan, G. J. Ball, A. R. Jamaluddin, and T. G. Leighton, Proc. R. Soc. A Math. Phys. Eng. Sci. **473**, 20170315 (2017).

[39] Y. A. Pishchalnikov, J. S. Neucks, R. J. VonDerHaar, I. V. Pishchalnikova, J. C. Williams, and J. A. McAteer, J. Urol. **176**, 2706 (2006).

[40] Y. A. Pishchalnikov, J. A. McAteer, J. S. Neucks, I. V. Pishchalnikova, and J. C. Williams, AIP Conf. Proc. **900**, 368 (2007).

[41] J. S. Neucks, Y. A. Pishchalnikov, A. J. Zancanaro, J. N. VonDerHaar, J. C. Williams, and J. A. McAteer, Urol. Res. **36**, 61 (2008).

[42] G. Li, J. C. Williams Jr, Y. A. Pishchalnikov, Z. Liu, and J. A. McAteer, BJU Int. **110**, E871 (2012).

[43] C. Bohris, A. Roosen, M. Dickmann, Y. Hocaoglu, S. Sandner, M. Bader, C. G. Stief, and S. Walther, J. Urol. **187**, 157 (2012).